

# PROSTATE SEGMENTATION IN MR IMAGES USING ENSEMBLE DEEP CONVOLUTIONAL NEURAL NETWORKS

Haozhe Jia<sup>1</sup>, Yong Xia<sup>1\*</sup>, Weidong Cai<sup>2</sup>, Michael Fulham<sup>1, 3, 4</sup>, David Dagan Feng<sup>2</sup>

1. Shaanxi Key Lab of Speech & Image Information Processing (SAIIP), School of Computer Science, Northwestern Polytechnical University, Xi'an 710072, China
  2. Biomedical and Multimedia Information Technology (BMIT) Research Group, School of Information Technologies, University of Sydney, NSW 2006, Australia
  3. Department of Molecular Imaging, Royal Prince Alfred Hospital, NSW 2050, Australia
  4. Sydney Medical School, University of Sydney, NSW 2006, Australia
- Email: [yxia@nwpu.edu.cn](mailto:yxia@nwpu.edu.cn)

## ABSTRACT

The automated segmentation of the prostate gland from MR images is increasingly used for clinical diagnosis. Since deep learning demonstrates superior performance in computer vision applications, we propose a coarse-to-fine segmentation strategy using ensemble deep convolutional neural networks (DCNNs) to address prostate segmentation in MR images. First, we use registration-based coarse segmentation on pre-processed prostate MR images to define the potential boundary region. We then train four DCNNs as voxel-based classifiers and classify the voxel in the potential region is a prostate voxel when at least three DCNNs made that decision. Finally, we use boundary refinement to eliminate the outliers and smooth the boundary. We evaluated our approach on the MICCAI PROMIS12 challenge dataset and our experimental results verify the effectiveness of the proposed algorithms.

**Index Terms**—MR prostate segmentation, deep convolutional neural network, voxel classification

## 1. INTRODUCTION

Statistics from National Cancer Institute indicate that greater than 220,800 men were diagnosed with prostate cancer in USA in 2015 [1] and they identify prostate cancer as a major health threat. Magnetic resonance (MR) imaging is the principal imaging technology for evaluation of the prostate gland due to its superior spatial resolution and tissue contrast [2]. Determination of the prostate volume and extension through the capsule of the gland is important for diagnosis, management and prognosis. Currently, MR prostate segmentation is mainly done by radiologists based almost entirely on visual inspection on a slice-by-slice basis, which is time-consuming, requires a high degree of skill, concentration, and is prone to intra- and inter-operator bias. Many semi or fully automated methods [3-5] have been proposed for segmentation of various organs or tissues from

medical images, however, automated MR prostate segmentation remains a challenging task. The challenges are largely related to the variability in size/shape/contours of the gland, heterogeneity in signal intensity around endorectal coils (ERCs) when used, imaging artifacts and low contrast between the gland and adjacent structures.

Recently, deep learning has been applied to a wide variety of problems, most prominently in computer vision, and it has been demonstrated that convolutional networks are advancing recognition. The availability of large annotated medical imaging data now makes it feasible to use deep convolutional neural networks (DCNNs) for medical image segmentation and classification [6].

In this paper, we propose a coarse-to-fine prostate segmentation approach that is based upon two components – an atlas-based coarse segmentation and an ensemble DCNN-based fine segmentation. We first perform the DRAMMS algorithm [7] to construct a probabilistic prostate atlas for coarse segmentation, and then train a set of DCNNs using the patches extracted from the boundary region obtained in coarse segmentation for fine segmentation. We evaluated our approach against several other state-of-the-art methods on the MICCAI PROMIS12 dataset [8].

## 2. ALGORITHM

The MR scans in the PROMIS12 dataset show marked variations in dynamic range, voxel size and appearance. Hence, in a pre-processing step we used the re-slicing procedure in the Statistical Parametric Mapping (SPM version 8)) [9] toolbox so that there was a uniform voxel size of  $0.7 \times 0.7 \times 2.2$  mm<sup>3</sup> for each scan. Then we separated the scans into those with ERCs and those without to reduce the impact of voxel values on the segmentation. The steps for both groups then comprised voxel value normalization, atlas-based coarse segmentation, ensemble DCNN-based fine segmentation and boundary refinement.



Fig. 1. An image slice from an ERC scan (left), the detected spike region (middle) and result from voxel value normalization (right).

### 2.1. Voxel Value Normalization

We used the following truncated linear map to normalize the voxel values of each non-ERCs studies:

$$I'_x = \begin{cases} 255 * \frac{(I_x - I_{min})}{(I_{max} - I_{min})}, & I_x \leq \tau \\ 255, & I_x \geq \tau \end{cases} \quad (1)$$

where  $I'_x$  is the normalized intensity of voxel  $x$ ,  $I_{max}$  and  $I_{min}$  are the maximum and minimum voxel values in the volume and  $\tau$  is the truncation threshold, which is empirically set to 4096 if  $I_{max} > 4096$  and 1024 otherwise.

ERC scans usually have intense spikes near the coil that may result in segmentation artifacts. We therefore applied the Poisson image editing [10] to each scan by: a) extracting the spike region near ERC using a threshold, whose value is equal to the truncation threshold  $\tau$  defined for non-ERC scans; b) converting the voxel value normalization problem into seeking an adjusted image,  $f: \Omega \mapsto R$ , so that the boundary of  $\Omega$  matches the spike region and the gradient within  $\Omega$  is similar to the high pass version of the image:

$$E(f) = \min \int_{\Omega} |\nabla f - \nabla g|^2 dx \quad (2)$$

where  $f = I$  on the boundary of the spike region and  $g(x) = (I - G_{\sigma} * I)(x)$  is the high pass filtered image. The minimizer of Eq. (2) is a solution to the Poisson equation:

$$\nabla^2 f = \nabla^2 g \quad (3)$$

c) using the voxel values on image  $f$  to replace the values in the bright region; and d) applying the adjusted voxel values to Eq. (1) to further normalize the scan. An example of an ERC image slice and the results from voxel value normalization are shown in Fig. 1. These images demonstrate that the heterogeneous signal intensity is substantially suppressed after the normalization.

### 2.2. Atlas-Based Coarse Segmentation

We constructed a probabilistic prostate atlas for each study and performed an atlas-based joint registration-comparison analysis to estimate the prostate volume. For each group of studies, let the scan to-be-segmented be denoted by  $S$ . Each

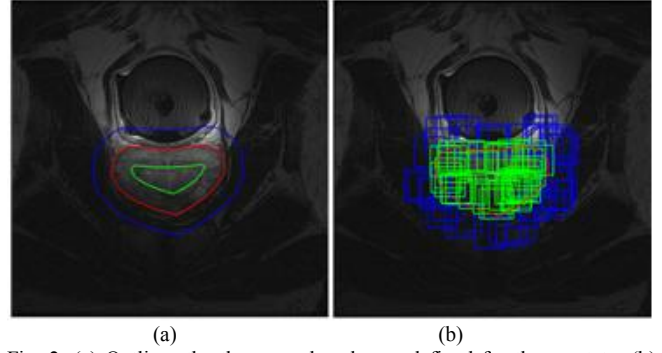


Fig. 2. (a) Outlines the three rough volumes defined for the prostate. (b) Prostate patches (green) and non-prostate patches (blue).

training case consisted of a co-aligned MR scan  $I_i$  and its binary segmentation ground truth  $L_i$ . We used the DRAMMS algorithm to modulate registration and to estimate a transformation  $T_i^{(S)}$  that maps the training scan  $I_i$  to the target scan  $S$ . Then we applied the transformation  $T_i^{(S)}$  to the ground truth  $L_i$ , and thus generated a prostate atlas  $A_i^{(S)}$  for  $S$ , in which each element  $a_{is}^{(S)} \in [0,1]$  gives the probability of the voxel  $s$  in  $S$  belonging to the prostate estimated according to the training scan  $I_i$ . The probability prostate atlas  $A^{(S)}$  was constructed by averaging the atlas produced by using all training cases to deal with the anatomical variation of human prostate gland. This probability atlas represents the heuristic knowledge provided by the training cases on the prior probability of each voxel belonging to the prostate gland.

Next, we applied a low threshold 0.25 and a high threshold 0.75 to the atlas and partitioned it into three regions, as shown in Fig. 2(a). The positive region is inside the lower boundary, which is highlighted in green, and gives the core volume of the prostate gland. The negative region is outside the higher boundary, which is highlighted in blue, and gives the background. The edges of prostate gland, outlined in red, are located in the annular boundary region, which lies between the green and the blue lines.

### 2.3. Ensemble DCNN-based Fine Segmentation

Since the distance between transverse slices is three times larger than the distance between two voxels within the slice, we perform boundary voxel classification on a slice-by-slice basis from the axial view.

For each voxel located in the boundary region on a training slice, we extracted a  $24 \times 24$  image patch that was centered on it as the input and used its class label as the output. In Fig. 2(b) prostate patches are highlighted in green and non-prostate patches in blue. We constructed an eight-layer DCNN, which consisted of three convolution layers, three pooling layers, two fully connected layers and is based on the MatConvNet [11]. The architecture and parameters of this DCNN are shown in Fig. 3.

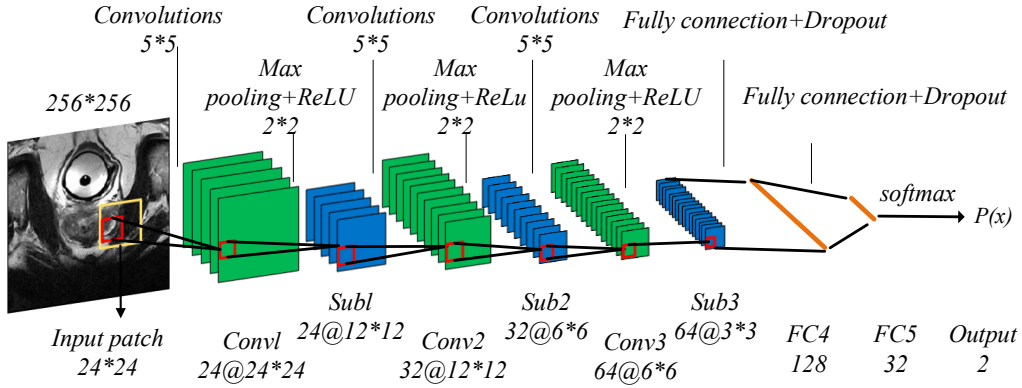


Fig. 3. Architecture of the proposed DCNNs.

To reduce the impact of the over-fitting on DCNN, we used independently sampled subsets of training data to train four DCNNs as weak classifiers and classified the voxels in the boundary volumes as prostate voxels when at least three of the four DCNNs make that prediction.

#### 2.4. Boundary Refinement

We applied a simple boundary refinement procedure to the raw output, since the temporary segmented images may have irregular region on the boundary. The operations involved in this process included  $3 \times 3$  median filtering, which removes isolated spurs and holes, and a boundary fitting procedure, which cleans up the boundary for an accurate and smooth segmentation result. In boundary fitting, we first calculate the distances between consecutive boundary points and the centroid, then remove 10% boundary points whose distance is most different from the mean distance, and finally fit a cubic B-spline to remaining boundary points to get the refined segmentation.

### 3. RESULTS

We applied our method on the all 50 training data of the dataset with 5-fold experiments. Segmentation results of our approach on central slices from different patients are shown in Fig. 4, where the obtained prostate boundary is highlighted in green and the ground truth boundary is marked in red. Although the obtained boundary was very near to the ground truth in most cases, there are mismatches in some locations. These inaccuracies can be largely ascribed to the potential complexity and similarity of soft tissues adjacent to the prostate, which may result in both over- and under-segmented boundaries.

In Table I, we report the mean and standard deviation of the Dice similarity coefficient (DSC), average boundary distance (ABD) and the 95% Hausdorff distance (95% HD) results that were obtained by applying our approach, the conventional active shape model (ASM), probabilistic ASM [12], 3D active appearance model (AAM) trained with and without ERC [13] to the PROMIS12 dataset. Our approach

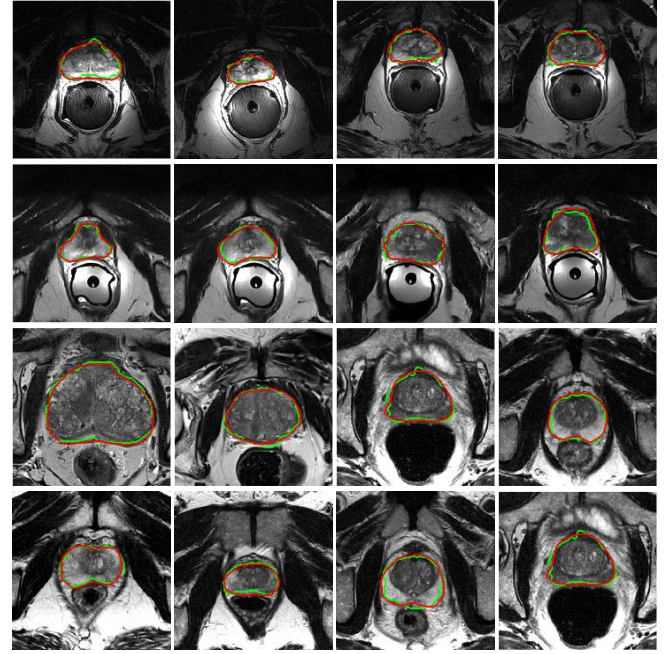


Fig. 4. Segmentation results of our approach on representative MR slices from different patients; the 'obtained' boundary is highlighted in green and the ground truth in red.

TABLE I  
MEAN±STANDARD DEVIATION OF SEGMENTATION ACCURACY

Algorithm	DSC	ABD (mm)	95%HD (mm)
Conventional ASM	0.78±0.01	3.12±1.71	/
Probabilistic ASM	0.86±0.01	<b>1.60±0.63</b>	/
3D AAM (1-shape model)	0.78±0.12	/	7.32±4.91
3D AAM (2-shape model)	0.81±0.12	/	6.43±4.63
Proposed	<b>0.88±0.04</b>	1.74±0.42	<b>5.00±1.25</b>

had the highest prostate segmentation accuracy in respect to DSC and 95%HD and the second most accurate segmentation when measured in terms of ABD.

TABLE II  
SEGMENTATION ACCURACY WHEN USING DIFFERENT PATCH SIZES

Data	Patch Size	DSC	ABD (mm)	95%HD (mm)	Network Training Time (h)
ERC	16 × 16	0.766	2.716	8.319	<b>2.0</b>
	24 × 24	<b>0.910</b>	<b>1.631</b>	<b>4.701</b>	2.5
	32 × 32	0.890	1.718	5.652	5.5
Non-ERC	16 × 16	0.793	2.782	7.591	<b>2.0</b>
	24 × 24	<b>0.887</b>	1.827	<b>5.348</b>	3.0
	32 × 32	0.885	<b>1.825</b>	5.452	6.0

The size of image patches can have a major impact on the accuracy of our approach. We randomly selected six ERC studies and six non-ERC studies as test cases and used other ERC and non-ERC studies as training cases to determine the optimal patch size. We set the size of image patches to 16 × 16, 24 × 24 and 32 × 32 and performed experiments on the two groups. The segmentation accuracy using the three metrics and the time cost for training are given in Table II, which shows that the 24 × 24 image patches achieved the most accurate segmentation and that increasing the patch size from 24 × 24 to 32 × 32 did not substantially improve the segmentation accuracy, but doubled the time cost for network training. The network training time here is off-line and not counted in the segmentation time. In the validation stage, the prediction of each image by the pre-trained network is less than 1 minute. Therefore, we set the size of image patches to 24 × 24 voxels in our experiments.

#### 4. CONCLUSIONS

We present an automated segmentation approach for prostate gland MR scans with and without ERC using the PROMIS12 dataset. The coarse segmentation was achieved by using a probabilistic prostate atlas constructed for each scan; the fine segmentation is accomplished by using a cohort of trained DCNNs. Our results suggest that DCNNs can substantially improve segmentation accuracy and our approach produced the highest accuracy when compared to the state-of-the-art approaches. Our future work will focus on: i) replacing DCNN with end-to-end deep models to avoid the construction of atlas; ii) adaptive decision fusion for deep learning; and iii) incorporating probability graph models as spatial constraints into the deep model-based segmentation to refine the boundary for improved segmentation.

#### 5. ACKNOWLEDGEMENT

This work was supported in part by the National Natural Science Foundation of China under Grants 61471297, in part by the Natural Science Foundation of Shaanxi Province, China under Grant 2015JM6287, and in part by the Australian Research Council (ARC) Grants. We appreciate the efforts devoted by the organizers of the 2012 Prostate MR Image Segmentation Challenge to collect and share the data for

comparing interactive and (semi)-automatic segmentation algorithms for MRI of the prostate.

#### 6. REFERENCES

- [1] R. L. Siegel, K. D. Miller, and A. Jemal, "Cancer statistics, 2015," *CA: a cancer journal for clinicians*, vol. 65, pp. 5-29, 2015.
- [2] J. L. Leake, R. Hardman, V. Ojili, I. Thompson, A. Shanbhogue, J. Hernandez, et al., "Prostate MRI: access to and current practice of prostate MRI in the United States," *Journal of the American College of Radiology*, vol. 11, pp. 156-160, 2014.
- [3] D. Stojanov and S. Koceski, "Topological MRI prostate segmentation method," in *FedCSIS 2014*, pp. 219-225, 2014.
- [4] M. Yang, X. Li, B. Turkbey, P. L. Choyke, and P. Yan, "Prostate segmentation in MR images using discriminant boundary features," *IEEE Transactions on Biomedical Engineering*, vol. 60, pp. 479-488, 2013.
- [5] Q. Gao, A. Asthana, T. Tong, Y. Hu, D. Rueckert, and P. J. Edwards, "Hybrid Decision Forests for Prostate Segmentation in Multi-channel MR Images," in *ICPR 2014*, pp. 3298-3303, 2014.
- [6] M. Havaei, A. Davy, D. Warde-Farley, A. Biard, A. Courville, Y. Bengio, et al., "Brain tumor segmentation with deep neural networks," *Medical Image Analysis*, 2016.
- [7] Y. Ou, A. Sotiras, N. Paragios, and C. Davatzikos, "DRAMMS: Deformable registration via attribute matching and mutual-saliency weighting," *Medical image analysis*, vol. 15, pp. 622-639, 2011.
- [8] G. Litjens, R. Toth, W. van de Ven, C. Hoeks, S. Kerkstra, B. van Ginneken, et al., "Evaluation of prostate segmentation algorithms for MRI: the PROMISE12 challenge," *Medical image analysis*, vol. 18, pp. 359-373, 2014.
- [9] K. J. Friston, A. P. Holmes, K. J. Worsley, J. P. Poline, C. D. Frith, and R. S. Frackowiak, "Statistical parametric maps in functional imaging: a general linear approach," *Human brain mapping*, vol. 2, pp. 189-210, 1994.
- [10] P. Pérez, M. Gangnet, and A. Blake, "Poisson image editing," in *ACM Transactions on Graphics (TOG)* 2003, pp. 313-318, 2003.
- [11] A. Vedaldi and K. Lenc, "Matconvnet: Convolutional neural networks for matlab," in *Proceedings of the 23rd ACM international conference on Multimedia 2015*, pp. 689-692, 2015.
- [12] M. Kirschner, F. Jung, and S. Wesarg, "Automatic prostate segmentation in MR images with a probabilistic active shape model," in *MICCAI 2012 Grand Challenge: Prostate MR Image Segmentation (PROMISE 2012)*, Oct. 1, 2012, Nice, France.
- [13] B. Maan and F. van der Heijden, "Prostate MR image segmentation using 3D active appearance models," in *MICCAI 2012 Grand Challenge: Prostate MR Image Segmentation (PROMISE 2012)*, Oct. 1, 2012, Nice, France.